

On the model-based design of front-to-total anti-roll moment distribution controllers for yaw rate tracking

M. Ricco, A. Percolla, G. Cardolini Rizzo, M. Zanchetta, D. Tavernini, M. Dhaens, M. Geraerts, A. Vigliani, A. Tota & A. Sorniotti

To cite this article: M. Ricco, A. Percolla, G. Cardolini Rizzo, M. Zanchetta, D. Tavernini, M. Dhaens, M. Geraerts, A. Vigliani, A. Tota & A. Sorniotti (2022) On the model-based design of front-to-total anti-roll moment distribution controllers for yaw rate tracking, *Vehicle System Dynamics*, 60:2, 569–596, DOI: [10.1080/00423114.2020.1825753](https://doi.org/10.1080/00423114.2020.1825753)

To link to this article: <https://doi.org/10.1080/00423114.2020.1825753>



© 2020 The Author(s). Published by Informa UK Limited, trading as Taylor & Francis Group



Published online: 21 Oct 2020.



Submit your article to this journal [↗](#)



Article views: 834



View related articles [↗](#)



View Crossmark data [↗](#)



Citing articles: 3 View citing articles [↗](#)

On the model-based design of front-to-total anti-roll moment distribution controllers for yaw rate tracking

M. Ricco^a, A. Percolla^a, G. Cardolini Rizzo^a, M. Zanchetta^a, D. Tavernini^a, M. Dhaens^b, M. Geraerts^b, A. Vigliani^c, A. Tota^c and A. Sorniotti^a

^aCentre for Automotive Engineering, University of Surrey, Guildford, UK; ^bAdvanced Chassis Research, Tenneco Automotive, Sint-Truiden, Belgium; ^cDepartment of Mechanical and Aerospace Engineering, Politecnico di Torino, Turin, Italy

ABSTRACT

In passenger cars active suspensions have been traditionally used to enhance comfort through body control, and handling through the reduction of the tyre load variations induced by road irregularities. However, active suspensions can also be designed to track a desired yaw rate profile through the control of the anti-roll moment distribution between the front and rear axles. The effect of the anti-roll moment distribution relates to the nonlinearity of tyre behaviour, which is difficult to capture in the linearised vehicle models normally used for control design. Hence, the tuning of anti-roll moment distribution controllers is usually based on heuristics. This paper includes an analysis of the effect of the lateral load transfer on the lateral axle force and cornering stiffness. A linearised axle force formulation is presented, and compared with a formulation from the literature, based on a quadratic relationship between cornering stiffness and load transfer. Multiple linearised vehicle models for control design are assessed in the frequency domain, and the respective controllers are tuned through optimisation routines. Simulation results from a nonlinear vehicle model are discussed to analyse the performance of the controllers, and show the importance of employing accurate models of the lateral load transfer effect during control design.

ARTICLE HISTORY

Received 18 February 2020
Revised 19 July 2020
Accepted 7 September 2020

KEYWORDS

active suspension; yaw rate control; linearisation; model-based design; stability

1. Introduction

Among their many functions, active suspension systems, either based on independent actuators at the vehicle corners or controllable anti-roll bars, are usually adopted to significantly reduce the roll motion caused by the lateral acceleration in cornering, through the generation of appropriate anti-roll moment. Moreover, these systems can also regulate the distribution of the anti-roll moment between the front and rear axles, which is directly related to the lateral load transfer distribution. The lateral load transfers deteriorate the lateral axle force capability, as the lateral force increment on the laden tyre is smaller than the lateral force decrease on the unladen tyre. Hence, when the load transfer is increased,

CONTACT A. Sorniotti  a.sorniotti@surrey.ac.uk

a larger slip angle is required to generate the same lateral axle force. Therefore, a front-to-total anti-roll moment distribution controller can vary the slip angle difference between the axles, i.e. the level of vehicle understeer, see [1–3]. For a given lateral acceleration, an increment of the load transfer on the front axle, with a corresponding decrement on the rear axle, increases understeer, which, viceversa, is reduced by an increase of the rear axle load transfer. Therefore, in quasi-steady-state cornering, active suspension control allows shaping the understeer characteristic and increasing the maximum achievable lateral acceleration, while during transients it can increase yaw and sideslip damping, and thus enhance active safety.

A rigorous optimisation-based analysis of the vehicle dynamics potential of active suspension systems is provided by the recent studies in [4,5]. Active suspensions have already been evaluated for yaw rate tracking, see [6–11]. For example, Varnhagen et al. [10] propose an active suspension controller based on the so-called cross-weight transfer parameter, which improves the lateral dynamics without affecting the chassis heave, pitch and roll dynamics. Yamamoto [11] compares the effect of different chassis control systems, including vertical tyre load distribution control, on the yaw and lateral dynamics in the linear and nonlinear regions of tyre operation.

The general trend towards model-based control requires simplified vehicle models for control development, or internal models for model predictive control. Furukawa et al. [12] assess the effectiveness of direct yaw moment control and active steering at high lateral accelerations, and state that ‘taking the nonlinearity of tyres and vehicle dynamics into consideration is essential for introducing the control law’. For example, with respect to modified single-track models, Badji et al. [13] propose a cubic formulation of the lateral axle force via a Taylor series expansion of the Pacejka magic formula. References [14–16] propose modified single-track model formulations, for reference cornering response generation, state estimation, and direct yaw moment control design, respectively. Although such models can well approximate the cornering response over the whole lateral acceleration range, they do not account for the lateral load transfer variations induced by active suspension actuators. In [17], while discussing linear vehicle models, Genta notes that ‘it is impossible to state the effect of anti-roll bars’ on the yaw rate, sideslip angle and lateral acceleration gains, ‘as they introduce a strong nonlinearity . . . and the very definition of the gains is based on a complete linearisation’.

Regarding model based suspension control, Jialing et al. [18] mention that, due to the important nonlinearity in the effect of the lateral load transfer on vehicle dynamics, it is necessary to formulate mathematical models that, although approximated, are still able to catch the fundamental effects of load transfer. In [6,7,19,20] the authors use the commonly adopted parabolic relationship between the individual vertical tyre load and its cornering stiffness, which brings a quadratic reduction of the axle cornering stiffness with the lateral load transfer. Chu et al. [19] investigate the relationship between the parabolic cornering stiffness and the resulting steady-state cornering response. Lakehal-Ayat et al. [21] adopt a nonlinear single-track vehicle model, with a combination of parabolic cornering stiffness and simplified Pacejka magic formula to describe the lateral axle force. In [22] Wu et al. use a vehicle model for suspension control design including consideration of the six degrees of freedom of the sprung mass; however, the linear relationship between slip angle and lateral tyre force, with constant cornering stiffness, cannot capture the effect of the anti-roll moment distribution on vehicle dynamics.

In summary, the previous simplified model formulations considering the anti-roll moment distribution effect are nonlinear, which poses an important limitation to their control design applicability; moreover, to our best knowledge, the implications of their linearisation have not been assessed in detail. Therefore, many authors use heuristics for the design of anti-roll moment distribution controllers. For example, on/off rules are proposed in [23]; in [24] the front-to-total anti-roll moment distribution ratio is proportional to the yaw rate error, with a gain depending on the lateral acceleration, while a fuzzy proportional–integral–derivative (PID) controller is adopted in [25]. In [26] Abe states that ‘as the effect of the lateral load transfer on the lateral/directional dynamics in itself is strongly nonlinear, it is difficult to derive the control law by using the fully analytical method. Therefore, this paper concentrates on computer simulation of vehicle response’ for control design. In [27], Cooper et al. explain that ‘the inverse model could not model the tyre nonlinearities sufficiently while still remaining simple enough Due to this, PID control was implemented for roll moment distribution’. Similarly, Yan et al. [28] report that ‘due to the nonlinear properties of four tires and the complicated dynamic information of the whole vehicle system, the distribution coefficient for yaw response characteristics is difficult to be accurately described, which means that the modern design method of control algorithm based on state equation is not applicable’. In the integrated chassis controller of [29], the front-to-total anti-roll moment distribution parameter is controlled through an empirical law, using a sideslip-based stability index and the yaw rate error, without model-based control. In [30] Ricco et al. present an anti-roll moment distribution controller consisting of nonlinear feedforward and linear feedback contributions; however, the study does not include the frequency response analysis of the model for feedback control design.

This paper aims to cover the identified gap, with the following contributions:

- The formulation of linearised vehicle models for anti-roll moment distribution control design, accounting for the variation of the lateral axle force and cornering stiffness with the lateral load transfer.
- The frequency domain comparison and critical analysis of the response of the proposed vehicle models.
- The performance evaluation, through an experimentally validated nonlinear vehicle simulation model, of the resulting model-based feedback controllers.

The manuscript is organised as follows: Section 2 analyses the lateral axle force behaviour with the load transfer, which is modelled with two alternative formulations in

Table 1. Main electric vehicle parameters.

Symbols	Description	Quantity
m	Vehicle mass	2530 kg
I_x	Roll mass moment of inertia	561 kg m ²
I_z	Yaw mass moment of inertia	3500 kg m ²
a_F	Front semi-wheelbase	1.559 m
a_R	Rear semi-wheelbase	1.374 m
h_{CG}	Centre of gravity height	0.720 m
t_F	Front track width	1.676 m
t_R	Rear track width	1.742 m
K_F	Front roll stiffness (passive components)	58,589 Nm/rad
K_R	Rear roll stiffness (passive components)	49,900 Nm/rad

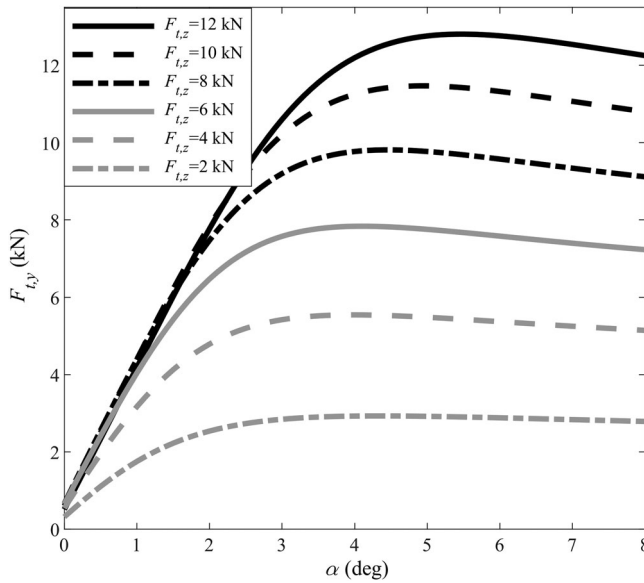


Figure 1. $F_{t,y}$ as a function of α , for different values of $F_{t,z}$, for a rear tyre of the case study vehicle.

Section 3; Section 4 describes the linearised vehicle dynamics models that are compared in the frequency domain in Section 5, and used to design proportional–integral (PI) front-to-total anti-roll moment distribution controllers in Section 6; finally, Section 7 assesses the controllers through vehicle dynamics simulations. All results refer to a case study sport utility electric vehicle with active suspension actuators, with the parameters reported in Table 1.

2. Effect of the lateral load transfer on the lateral axle force and cornering stiffness

Figure 1 shows the variation of the lateral tyre force, $F_{t,y}$, as a function of slip angle, α , for different values of vertical load, $F_{t,z}$, by using the Pacejka magic formula (version 5.2), parametrised for the rear tyres of the case study vehicle, for slip ratio and camber angle equal to zero. The lateral tyre force gradient decreases with α , and eventually becomes negative for the specific tyre, once force saturation occurs. In general, for typical passenger car tyres, it can be observed that lateral force saturation happens at larger slip angles, for increasing values of $F_{t,z}$. Moreover, very importantly, for a fixed value of α , $F_{t,y}$ varies with $F_{t,z}$ in a nonlinear fashion, i.e. the increment of $F_{t,y}$ is less than proportional to the increment of $F_{t,z}$. Hence, an accurate estimation of the lateral axle force must consider the lateral load transfer during cornering.

To a first approximation, the lateral load transfer within an axle is defined as [17]:

$$\Delta F_{z,i} = \frac{m a_y [l - a_i] d_i}{l t_i} + \frac{M_{AR, Tot, i}}{t_i} \quad (1)$$

where the subscript $i = F, R$ refers to the front (F) and rear (R) axles; m is the vehicle mass (the distinction between sprung and unsprung mass is neglected); a_y is the lateral

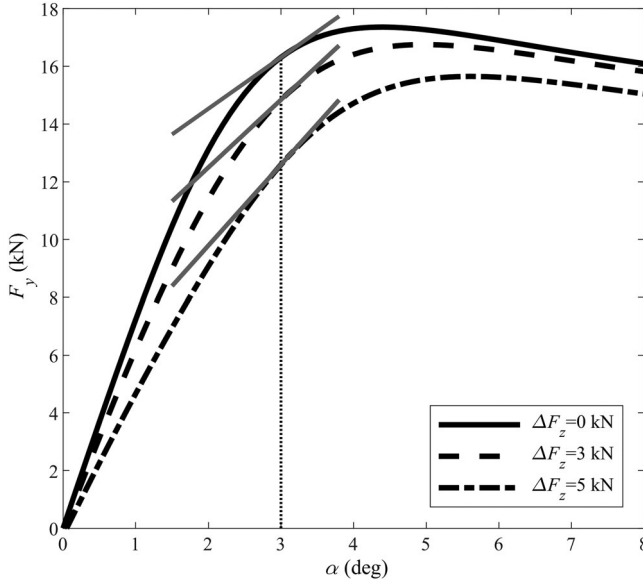


Figure 2. F_y as a function of α , for different values of ΔF_z , for the rear axle of the case study vehicle.

acceleration; l is the wheelbase; a_i is the semi-wheelbase, i.e. the longitudinal distance between the axle and the centre of gravity; d_i is the roll centre height; t_i is the track width; $M_{AR,Tot,i}$ is the total anti-roll moment of the axle's suspension, including the effect of springs, dampers, anti-roll bars and controlled actuators.

During cornering at constant vehicle speed, the vertical loads on the left (L) and right (R) tyres of i -th axle, $F_{t,z,iL}$ and $F_{t,z,iR}$, are:

$$\begin{aligned} F_{t,z,iL} &= \frac{1}{2}F_{z,i,0} + \Delta F_{z,i} \\ F_{t,z,iR} &= \frac{1}{2}F_{z,i,0} - \Delta F_{z,i} \end{aligned} \quad (2)$$

where $F_{z,i,0}$ is the static axle load. For the tyre parametrisation of Figure 1, Figure 2 reports the lateral axle force, $F_{y,i}$, as a function of α_i , for constant lateral load transfer values, $\Delta F_{z,i}$, according to (2):

$$F_{y,i}(\alpha_i, \Delta F_{z,i}) = F_{t,y,iL}(\alpha_i, F_{t,z,iL}) + F_{t,y,iR}(\alpha_i, F_{t,z,iR}) \quad (3)$$

where the notation (\cdot) in (3) and in the remainder indicates a function.

In this study, the axle cornering stiffness, C_i , calculated at α_i for a fixed $\Delta F_{z,i}$, is defined as the gradient of the lateral axle force characteristic:

$$C_i(\alpha_i, \Delta F_{z,i}) = \frac{F_{y,i}(\alpha_i + \Delta\alpha, \Delta F_{z,i}) - F_{y,i}(\alpha_i, \Delta F_{z,i})}{\Delta\alpha} \quad (4)$$

where $\Delta\alpha$ is a small slip angle increment. This definition of cornering stiffness is an extension of the classical one from the literature, which refers to the condition of zero slip angle. Such broader definition of C_i is needed for the analysis of front-to-total anti-roll moment distribution controllers, as this typology of actuation tends to be effective only at medium-to-high lateral accelerations and slip angles, i.e. rather far from the condition

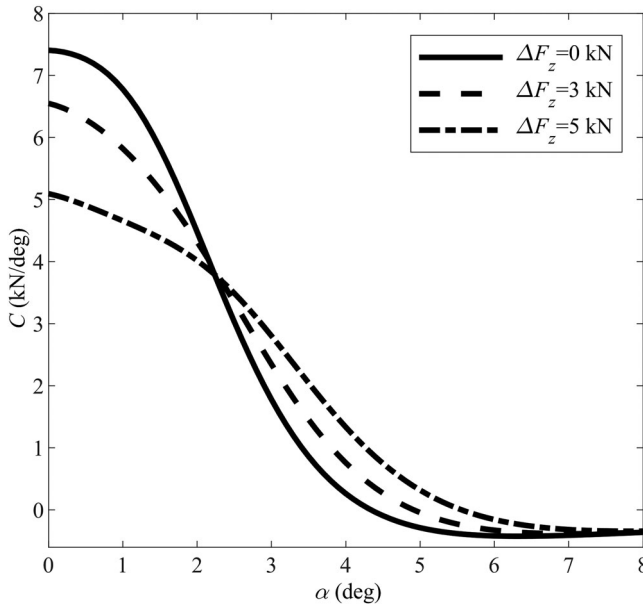


Figure 3. C as a function of α , for different values of ΔF_z , for the rear axle of the case study vehicle.

$\alpha_i = 0$. Figure 3 plots C_i as a function of α_i , for the same values of $\Delta F_{z,i}$ as in Figure 2, by using $\Delta\alpha = 0.5$ deg.

As expected, the lateral axle force always decreases with the lateral load transfer increase (see Figure 2), while – very interestingly, as it contradicts the common belief – the axle cornering stiffness increases with the load transfer increase for medium-to-high slip angles, see the slopes of the tangent lines to the lateral axle force characteristics in Figure 2, and the cornering stiffness plots in Figure 3. This behaviour is confirmed by the curves at constant ΔF_z in the right subplot of Figure 4, in which the inclination of the lateral axle force characteristics increases with the lateral load transfer increase, starting from slip angles of approx. 2.1 deg. During the study, the analysis of the lateral force behaviour of a variety of tyres brought the important and general conclusion that, for considerable slip angles, the increase of the axle cornering stiffness with the increase of the lateral load transfer is a common characteristic of passenger car tyres of any size. The physical reason is that tyre saturation occurs at higher values of slip angle when the vertical tyre load is increased, i.e. the cornering stiffness of the outer tyre of the axle tends to remain positive for a larger range of slip angles, if the lateral load transfer increases.

During vehicle's operation, the situation is further complicated by the fact that the lateral load transfer and slip angle concurrently change with the lateral acceleration, a_y . To a first approximation, in steady-state cornering, $M_{AR,Tot,i}$ is directly proportional to a_y , and therefore (1) can be simplified into:

$$\begin{aligned}\Delta F_{z,F} &\approx \chi \frac{m a_y h_{CG}}{t_F} \\ \Delta F_{z,R} &\approx [1 - \chi] \frac{m a_y h_{CG}}{t_R}\end{aligned}\quad (5)$$

where h_{CG} is the centre of gravity height and χ is the front-to-total lateral load transfer distribution parameter, which depends on the suspension set-up. From the lateral force

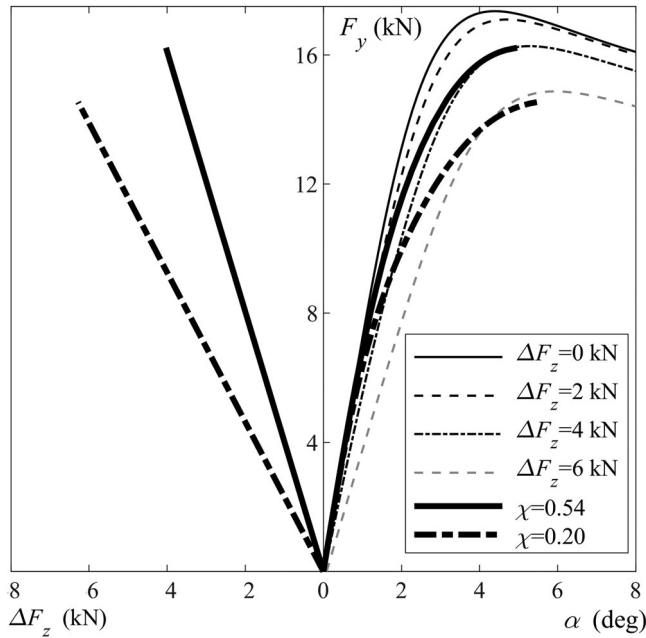


Figure 4. F_y as a function of ΔF_z and α , for the rear axle of the case study vehicle.

and yaw moment balance equations in steady-state cornering, under the assumption of zero direct yaw moment, (5) becomes:

$$\begin{aligned} \Delta F_{z,F} &\approx \chi \frac{F_{y,F} l_{hCG}}{a_R t_F} \\ \Delta F_{z,R} &\approx [1 - \chi] \frac{F_{y,R} l_{hCG}}{a_F t_R} \end{aligned} \quad (6)$$

which shows the linear proportionality between the load transfer and the respective lateral axle force (for a given χ value), depicted in the left subplot of Figure 4 (see also [31]). Therefore, in steady-state cornering, the lateral axle force characteristic follows profiles like those indicated in Figure 4 by $\chi = 0.54$ and $\chi = 0.20$, each corresponding to a different suspension set-up.

The important conclusion is that the main consequence of the lateral load transfer is the reduction of the lateral axle force at the specific slip angle, while the cornering stiffness variation is a secondary effect, and can be either in the direction of an increase or decrease. This rather complex behaviour cannot be represented by the conventional parabolic formulation in [6], which considers a quadratic decrease of the axle cornering stiffness with the lateral load transfer. Hence, an accurate yet simple and linear model of the lateral axle force is needed for the model-based design of anti-roll moment distribution controllers in the frequency domain.

3. Lateral axle force models

3.1. Proposed lateral axle force model (Model A)

The proposed model, called Model A in the remainder, expresses the relationship between $F_{y,i}$, α_i and $\Delta F_{z,i}$, around a linearisation point defined by $F_{y,i,0}$, $\alpha_{i,0}$ and $\Delta F_{z,i,0}$,

corresponding to an axle cornering stiffness $C_{i,0}$ defined as in (4). For a given $\Delta F_{z,i}$, $F_{y,i}$ is represented as a linear function of α_i :

$$F_{y,i} \approx F_{y,i,lin} + C_i[\alpha_i - \alpha_{i,0}] \quad (7)$$

In accordance to Figures 2 and 3, both $F_{y,i,lin}$ and C_i vary with $\Delta F_{z,i}$, which can be expressed through a first order Taylor series expansion around $\Delta F_{z,i,0}$:

$$\begin{aligned} F_{y,i,lin} &\approx F_{y,i,0} + F'_{y,i,0}[\Delta F_{z,i} - \Delta F_{z,i,0}] \\ C_i &\approx C_{i,0} + C'_{i,0}[\Delta F_{z,i} - \Delta F_{z,i,0}] \end{aligned} \quad (8)$$

where $F'_{y,i,0}$ and $C'_{i,0}$ are the gradients of the lateral axle force and axle cornering stiffness with respect to the load transfer, which can be derived from Figures 2 and 3. By combining (7) and (8), the complete formulation becomes:

$$F_{y,i} \approx F_{y,i,0} + F'_{y,i,0}[\Delta F_{z,i} - \Delta F_{z,i,0}] + \{C_{i,0} + C'_{i,0}[\Delta F_{z,i} - \Delta F_{z,i,0}]\}[\alpha_i - \alpha_{i,0}] \quad (9)$$

3.2. Parabolic lateral axle force model (Model B)

Model B is based on (7), where C_i is given by

$$C_i = c_{1,i}[F_{t,z,iL} + F_{t,z,iR}] + c_{2,i}[F_{t,z,iL}^2 + F_{t,z,iR}^2] \quad (10)$$

By substituting (10) into (7), using (2), and imposing $F_{y,i,lin} = F_{y,i,0}$, the following formulation is obtained:

$$\begin{aligned} F_{y,i} &\approx F_{y,i,lin} + \{c_{1,i}[F_{t,z,iL} + F_{t,z,iR}] + c_{2,i}[F_{t,z,iL}^2 + F_{t,z,iR}^2]\}[\alpha_i - \alpha_{i,0}] \\ &= F_{y,i,0} + \left[c_{1,i}F_{z,i,0} + \frac{1}{2}c_{2,i}F_{z,i,0}^2 + 2c_{2,i}\Delta F_{z,i}^2 \right] [\alpha_i - \alpha_{i,0}] \end{aligned} \quad (11)$$

For $\alpha_{i,0} = 0$ and $F_{y,i,0} = 0$, Model B becomes the common parabolic model [6,7,19,20]:

$$F_{y,i} = \left[c_{1,i}F_{z,i,0} + \frac{1}{2}c_{2,i}F_{z,i,0}^2 + 2c_{2,i}\Delta F_{z,i}^2 \right] \alpha_i \quad (12)$$

In the literature, $c_{1,i}$ and $c_{2,i}$ have opposite signs, i.e. an increment in the lateral load transfer always leads to a decrement of the axle cornering stiffness, and therefore of the lateral force. However, in reality, as discussed for Figures 2 and 3, at medium-to-high slip angles, an increased lateral load transfer can lead to increased axle cornering stiffness.

In this study, the values of $c_{1,i}$ and $c_{2,i}$ were computed to match: (i) the $C_{i,0}$ value obtained from the magic formula at the selected linearisation point through (4); and (ii) the axle cornering stiffness value, $C_{i,0}^*$, obtained from the magic formula at the same slip angle as in (i), but at a second lateral load transfer, $\Delta F_{z,i}^*$ ($\Delta F_{z,i}^* = \Delta F_{z,i,0} + 500$ N in the calculations). Hence, a system of two equations outputs $c_{1,i}$ and $c_{2,i}$:

$$\begin{cases} C_{i,0} = c_{1,i}F_{z,i,0} + \frac{1}{2}c_{2,i}F_{z,i,0}^2 + 2c_{2,i}\Delta F_{z,i}^2 \\ C_{i,0}^* = c_{1,i}F_{z,i,0} + \frac{1}{2}c_{2,i}F_{z,i,0}^2 + 2c_{2,i}\Delta F_{z,i}^{*2} \end{cases} \quad (13)$$

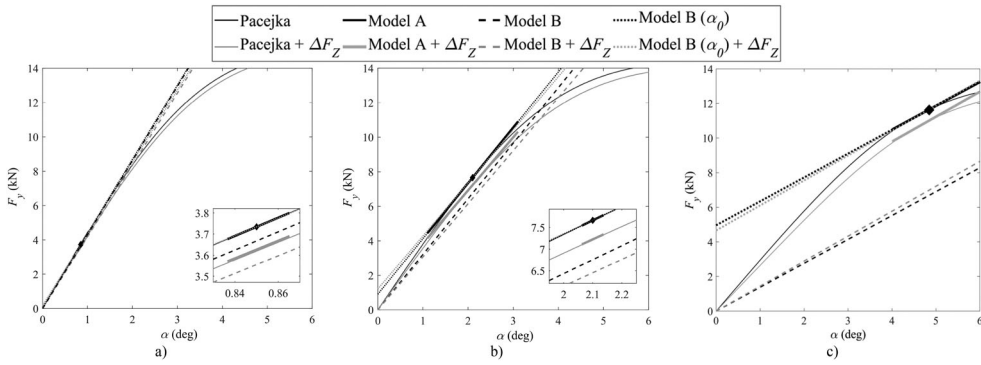


Figure 5. Comparison of the $F_y(\alpha)$ characteristics of the rear axle of the case study vehicle, obtained from the magic formula, Model A and Model B, for steady-state cornering at: (a) $a_y = 3 \text{ m/s}^2$; (b) $a_y = 6 \text{ m/s}^2$; and (c) $a_y = 9 \text{ m/s}^2$.

3.3. Lateral axle force model comparison

Figure 5 compares the lateral axle force characteristics from the magic formula, Model A and Model B. The reference operating points, highlighted by the square markers, are defined for nominal values of $F_{y,i,0}$, $\alpha_{i,0}$ and $\Delta F_{z,i,0}$, corresponding to $a_y = 3, 6$ and 9 m/s^2 , obtained for steady-state cornering through the quasi-static model in [30,32–34]. For all models, the results are reported for: (i) $\Delta F_{z,i} = \Delta F_{z,i,0}$; and (ii) $\Delta F_{z,i}^* = \Delta F_{z,i,0} + \Delta F_z$, with $\Delta F_z = 500 \text{ N}$, which corresponds to the notation ‘ $+\Delta F_z$ ’ in the legend. Moreover, for Model B, the graphs are for: (a) the formulation described by (12) (indicated as Model B in the plots), typical of the literature; and (b) the complete formulation in (11), with a linearisation at the operating point specified by the quasi-static model (indicated as Model B (α_0)).

Model A provides a consistently accurate approximation of the magic formula around the nominal point, for both slip angle and load transfer variations. At 6 and 9 m/s^2 , Model B significantly underestimates the lateral axle force at the reference operating point, because of its linearisation at the origin, while Model B (α_0) overestimates the axle lateral force at $\Delta F_{z,i}^*$, as it considers only the axle cornering stiffness variation with the load transfer, and not the axle force variation at the linearisation point. To the purpose of control design in the frequency domain, where only the variation of the relevant variables with respect to a reference point matters, Model B and Model B (α_0) provide identical outputs, as their cornering stiffness values are the same. Therefore, Model B (α_0) will be omitted from the following analyses.

4. Linearised vehicle dynamics models for control design

This section introduces four linearised vehicle dynamics models for anti-roll moment distribution control design, i.e. Models 1–4. The models are modified versions of the well-known single-track model for constant speed conditions [35], and include consideration of the lateral load transfer variations caused by active suspensions. The main characteristics are summarised in Table 2, where f is the front-to-total anti-roll moment distribution

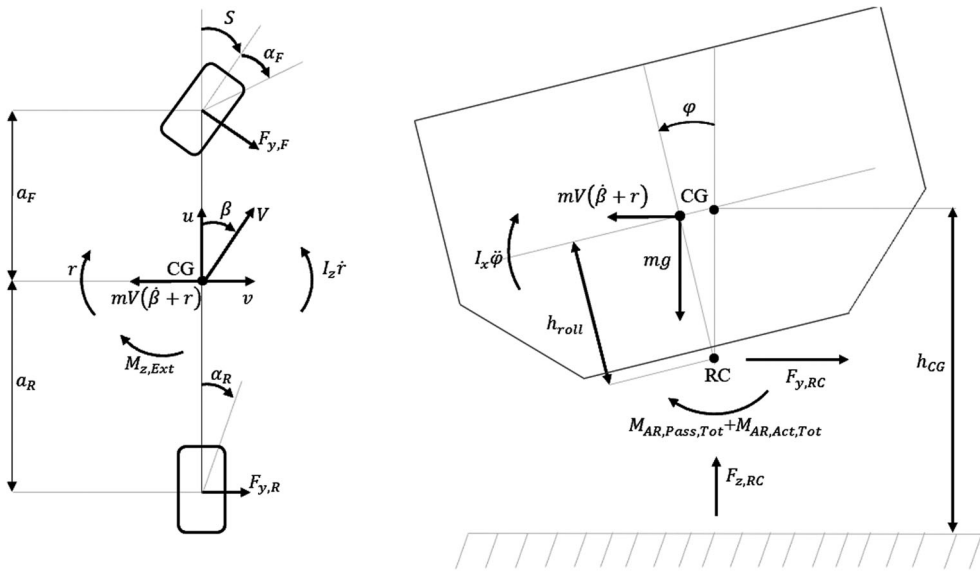


Figure 6. Simplified top and rear views of the vehicle, with indication of the sign conventions, main variables and parameters.

Table 2. Main characteristics of Models 1–4.

Vehicle model no.	States	Lateral axle force model	Load transfer model	Total active anti-roll moment
1	$\beta, r, \varphi, \dot{\varphi}$	Model A	Based on $\varphi, \dot{\varphi}$ and $M_{AR,Act,i}$	Based on a_y
2	$\beta, r, \varphi, \dot{\varphi}$	Model A	Based on $\varphi, \dot{\varphi}$ and $M_{AR,Act,i}$	Based on r
3	$\beta, r, \varphi, \dot{\varphi}$	Model A	Based on $\varphi, \dot{\varphi}$ and $M_{AR,Act,i}$	Based on φ and $\dot{\varphi}$
4	β, r	Model B	Based on r and f	Based on r

factor of the active contribution (see Figure 6 for the notations); in particular, for the lateral axle force, Models 1–3 use Model A, while Model 4 adopts Model B.

4.1. Model 1

This model has three degrees of freedom, i.e. it is based on the lateral force, yaw moment and roll moment balance equations:

$$\begin{cases} mV[\dot{\beta} + r] = F_{y,F} + F_{y,R} \\ I_z \dot{r} = F_{y,F}a_F - F_{y,R}a_R + M_{z,Ext} \\ I_x \ddot{\varphi} = mV[\dot{\beta} + r]h_{roll} + mgh_{roll}\varphi - M_{AR,Pass,F} - M_{AR,Pass,R} - M_{AR,Act,F} - M_{AR,Act,R} \end{cases} \quad (14)$$

where V is the vehicle speed; r is the yaw rate; $\dot{\beta}$ is the sideslip rate; I_z is the yaw mass moment of inertia; $M_{z,Ext}$ is an external yaw moment, e.g. caused by direct yaw moment control through the friction brakes or torque-vectoring; I_x is the roll mass moment of inertia; φ is the roll angle; h_{roll} is the distance between the centre of gravity and roll axis; g is the gravitational acceleration; $M_{AR,Pass,F}$ and $M_{AR,Pass,R}$ are the front and rear passive anti-roll moment contributions; and $M_{AR,Act,F}$ and $M_{AR,Act,R}$ are the front and rear active anti-roll moment contributions.

The passive anti-roll moments are described by

$$\begin{aligned} M_{AR,Pass,F} &= K_F\varphi + D_F\dot{\varphi} \\ M_{AR,Pass,R} &= K_R\varphi + D_R\dot{\varphi} \end{aligned} \quad (15)$$

where K_F and K_R are the front and rear axle roll stiffness values, and D_F and D_R are the respective roll damping coefficients.

Model 1 expresses the active anti-roll moments as functions of lateral acceleration:

$$\begin{aligned} M_{AR,Act,F} &= kma_y h_{roll} f = kmV[\dot{\beta} + r]h_{roll} f \\ M_{AR,Act,R} &= kma_y h_{roll} [1 - f] = kmV[\dot{\beta} + r]h_{roll} [1 - f] \end{aligned} \quad (16)$$

where $ma_y h_{roll}$ is the total roll moment caused by the vehicle's lateral acceleration; the gain k indicates the level of roll moment compensation of the active suspension system, i.e. $k = 0$ indicates no compensation and $k = 1$ indicates full compensation; and f is the control input, i.e. the ratio between the front active anti-roll moment and total active anti-roll moment:

$$f = \frac{M_{AR,Act,F}}{M_{AR,Act,Tot}} = \frac{M_{AR,Act,F}}{M_{AR,Act,F} + M_{AR,Act,R}} \quad (17)$$

Under the small angle approximation, the front and rear axle slip angles are:

$$\begin{aligned} \alpha_F &\approx \beta + \frac{a_F}{V}r - S \\ \alpha_R &\approx \beta - \frac{a_R}{V}r \end{aligned} \quad (18)$$

where S is the steering angle. The effects of roll steer and camber angle are neglected, which is rather common and reasonable approximation in simplified models for control system design, also considering the reduced roll angle values brought by the active suspension system, and the generally very limited effect of camber angle – in comparison with slip angle – on the lateral tyre forces in passenger cars.

The lateral load transfer is calculated with (1), with $M_{AR,Tot,i} = M_{AR,Pass,i} + M_{AR,Act,i}$. As for the case study vehicle the roll axis is very close to the ground, in the following formulations it is imposed $h_{roll} = h_{CG}$ (Figure 6).

By substituting (1) and (15)–(18) into (9), the front and rear lateral axle forces become:

$$\begin{aligned} F_{y,F} &\approx F_{y,F,0} + F'_{y,F,0} \left\{ \frac{fh_{CG}mV[\dot{\beta} + r]k + K_F\varphi + D_F\dot{\varphi}}{t_F} - \Delta F_{z,F,0} \right\} \\ &\quad + \left[\beta + \frac{a_F}{V}r - S - \alpha_{F,0} \right] \\ &\quad \left\{ C_{F,0} + C'_{F,0} \left\{ \frac{fh_{CG}mV[\dot{\beta} + r]k + K_F\varphi + D_F\dot{\varphi}}{t_F} - \Delta F_{z,F,0} \right\} \right\} \\ F_{y,R} &\approx F_{y,R,0} + F'_{y,R,0} \left\{ \frac{[1 - f]h_{CG}mV[\dot{\beta} + r]k + K_R\varphi + D_R\dot{\varphi}}{t_R} - \Delta F_{z,R,0} \right\} \\ &\quad + \left[\beta - \frac{a_R}{V}r - \alpha_{R,0} \right] \\ &\quad \left\{ C_{R,0} + C'_{R,0} \left\{ \frac{[1 - f]h_{CG}mV[\dot{\beta} + r]k + K_R\varphi + D_R\dot{\varphi}}{t_R} - \Delta F_{z,R,0} \right\} \right\} \end{aligned} \quad (19)$$

By re-arranging (14)–(19), the model equations are obtained, where the state, input, disturbance and output vectors, respectively x , u , w and y , are:

$$x = \begin{bmatrix} \beta \\ r \\ \varphi \\ \dot{\varphi} \end{bmatrix}, \quad u = [f], \quad w = \begin{bmatrix} S \\ M_{z,Ext} \end{bmatrix}, \quad y = \begin{bmatrix} \beta \\ r \\ \varphi \\ a_y \\ \Delta F_{z,F} \\ \Delta F_{z,R} \end{bmatrix} \quad (20)$$

S and $M_{z,Ext}$ are considered disturbances as they are not calculated by the controller; however, the input vector can be augmented with additional control inputs, such as the front and rear steering angles and direct yaw moment. The system equations are expressed in the compact form:

$$\begin{cases} \dot{x} = q(x, u, w) \\ y = h(x, u, w) \end{cases} \quad (21)$$

Differently from the conventional single-track model formulation, (21) is nonlinear, because of the terms related to: (i) the suspension control action, f ; (ii) the variation of the lateral axle force with the lateral load transfer, $F'_{y,i,0}$; and (iii) the variation of the cornering stiffness with the lateral load transfer, $C'_{y,i,0}$. The system variables are expressed with respect to the linearisation point:

$$x = x_0 + \delta x \quad u = u_0 + \delta u \quad w = w_0 + \delta w \quad y = y_0 + \delta y \quad (22)$$

where x_0 , u_0 , w_0 and y_0 are the vector values at the linearisation point, and the symbol δ indicates a deviation. Then the linearisation of (21) is:

$$\begin{cases} \dot{x}_0 + \delta \dot{x} = q(x_0, u_0, w_0) + \left. \frac{\partial q}{\partial x} \right|_{\delta x=0} \delta x + \left. \frac{\partial q}{\partial u} \right|_{\delta x=0} \delta u + \left. \frac{\partial q}{\partial w} \right|_{\delta x=0} \delta w \\ y_0 + \delta y = h(x_0, u_0, w_0) + \left. \frac{\partial h}{\partial x} \right|_{\delta x=0} \delta x + \left. \frac{\partial h}{\partial u} \right|_{\delta x=0} \delta u + \left. \frac{\partial h}{\partial w} \right|_{\delta x=0} \delta w \end{cases} \quad (23)$$

As $\dot{x}_0 = q(x_0, u_0, w_0)$ and $y_0 = h(x_0, u_0, w_0)$, the linearised system becomes:

$$\begin{cases} \delta \dot{x} = A\delta x + B\delta u + E\delta w \\ \delta y = C\delta x + D\delta u + F\delta w \end{cases} \quad (24)$$

where A , B and E are the state, input and disturbance matrices, and C , D and F are the respective output equation matrices. In the equations, $\alpha_{i,0}$, $\Delta F_{z,i,0}$, r_0 and f_0 are obtained from the nonlinear quasi-static model from [30], suitable for the analysis of the steady-state cornering behaviour; $F_{y,i,0}$, $F'_{y,i,0}$ and $C'_{i,0}$ are calculated through the manipulation of the magic formula, whereas β_0 , φ_0 and S_0 result from (21), by imposing $q(x_0, u_0, w_0) = 0$.

4.2. Model 2

Model 2 is based on the same equations as Model 1, apart from the definition of the active anti-roll moments, which uses the steady-state relationship between yaw rate and lateral acceleration, i.e. $a_y \approx Vr$:

$$\begin{aligned} M_{AR,Act,F} &= fh_{CG}mVrk \\ M_{AR,Act,R} &= [1 - f]h_{CG}mVrk \end{aligned} \quad (25)$$

4.3. Model 3

Model 3 uses the same equations as Model 1, apart from the definition of the active anti-roll moments, which are expressed as functions of roll angle and roll rate via the total active roll stiffness, K_{Tot} , and total active roll damping coefficient, D_{Tot} , which are designed to provide the desired roll angle characteristic and corresponding roll damping ratio:

$$\begin{aligned} M_{AR,Act,F} &= f[K_{Tot}\varphi + D_{Tot}\dot{\varphi}] \\ M_{AR,Act,R} &= [1 - f][K_{Tot}\varphi + D_{Tot}\dot{\varphi}] \end{aligned} \quad (26)$$

4.4. Model 4

Model 4 uses Model B's quadratic formulation of the lateral axle force (see Section 3). Consistently with the literature (e.g. see [6]), only the lateral force and yaw moment balance equations are included in the model:

$$\begin{cases} mV[\dot{\beta} + r] = F_{y,F} + F_{y,R} \\ I_z\dot{r} = F_{y,F}a_F - F_{y,R}a_R + M_{z,Ext} \end{cases} \quad (27)$$

The vertical tyre forces are given by

$$\begin{aligned} F_{t,z,FL} &= \frac{1}{2}F_{z,F,0} + \Delta F_{z,F} = \frac{1}{2}F_{z,F,0} + mV\frac{h_{CG}}{t_F}r \left\{ \frac{K_F[1 - k]}{K_F + K_R} + kf \right\} \\ F_{t,z,FR} &= \frac{1}{2}F_{z,F,0} - \Delta F_{z,F} = \frac{1}{2}F_{z,F,0} - mV\frac{h_{CG}}{t_F}r \left\{ \frac{K_F[1 - k]}{K_F + K_R} + kf \right\} \\ F_{t,z,RL} &= \frac{1}{2}F_{z,R,0} + \Delta F_{z,R} = \frac{1}{2}F_{z,R,0} + mV\frac{h_{CG}}{t_R}r \left\{ \frac{K_R[1 - k]}{K_F + K_R} + k[1 - f] \right\} \\ F_{t,z,RR} &= \frac{1}{2}F_{z,R,0} - \Delta F_{z,R} = \frac{1}{2}F_{z,R,0} - mV\frac{h_{CG}}{t_R}r \left\{ \frac{K_R[1 - k]}{K_F + K_R} + k[1 - f] \right\} \end{aligned} \quad (28)$$

By defining:

$$\begin{aligned} C_{F,0} &= c_{1,F}F_{z,F,0} + \frac{1}{2}c_{2,F}F_{z,F,0}^2 \\ C_{R,0} &= c_{1,R}F_{z,R,0} + \frac{1}{2}c_{2,R}F_{z,R,0}^2 \end{aligned} \quad (29)$$

where $C_{F,0}$ and $C_{R,0}$ represent the front and rear axle cornering stiffness at zero lateral load transfer, the lateral axle forces from (12) can be rewritten in compact form as

$$\begin{cases} F_{y,F} = \alpha_F[C_{F,0} + 2c_{2,F}\Delta F_{z,F}^2] \\ F_{y,R} = \alpha_R[C_{R,0} + 2c_{2,R}\Delta F_{z,R}^2] \end{cases} \quad (30)$$

The Model 4 equations result in:

$$\begin{cases} \dot{\beta} = \frac{1}{mV} \{ [\beta + \frac{a_F}{V} r - S] [C_{F,0} + 2c_{2,F} \Delta F_{z,F}^2] + [\beta - \frac{a_R}{V} r] [C_{R,0} + 2c_{2,R} \Delta F_{z,R}^2] \} - r \\ \dot{r} = \frac{1}{I_z} \{ [\beta + \frac{a_F}{V} r - S] [C_{F,0} + 2c_{2,F} \Delta F_{z,F}^2] a - [\beta - \frac{a_R}{V} r] [C_{R,0} + 2c_{2,R} \Delta F_{z,R}^2] b + M_{z,Ext} \} \end{cases} \quad (31)$$

Similarly to Models 1–3, Model 4 is linearised and expressed in state-space form, where β and r are the states, f is the input, and S and $M_{z,Ext}$ are the disturbances.

5. Frequency domain analyses and comparisons

5.1. Model 1 analysis

Figure 7 is an example of sensitivity analysis with Model 1 in the frequency domain, for different values of k , with δf as input. For $k = 0$, there is not any active anti-roll moment contribution, hence δf does not have any effect. For $k \neq 0$, δf influences the load transfers (see Figure 7(e,f)); in particular, in steady-state, the phase angles ϕ of $\delta \Delta F_{z,F}$ and $\delta \Delta F_{z,R}$ are respectively 0 and -180 deg, i.e. a positive δf increases the front anti-roll moment and decreases the rear anti-roll moment, which, in accordance with the phase angles, leads to positive $\delta \Delta F_{z,F}$ and negative $\delta \Delta F_{z,R}$. From the phase plots of Figure 7(a,b), a positive variation of the anti-roll moment distribution provokes a negative variation of the yaw rate, δr , and lateral acceleration, δa_y , which means that the vehicle becomes more understeering, consistently with the discussion in Section 1.

The magnitude plots show that an increase of k increases the sensitivity of the variables to δf . The only exception is represented by the roll angle. For small values of k , the magnitude of $\delta \varphi$ increases with k (Figure 7(d)). In fact, in these conditions, the magnitude increase of δa_y induced by δf provokes an amplitude increase of $\delta \varphi$; such effect prevails over the $\delta \varphi$ magnitude reduction associated with the increased active anti-roll moment caused by the increasing values of k . However, for large values of k , the roll angle magnitude is so low that is not significantly influenced by the lateral acceleration variation induced by δf anymore; hence, the $\delta \varphi$ magnitude decreases with the increase of k . The cases at $k = 1.0$ and $k = 1.2$ are interesting in terms of $\delta \varphi$. For $k = 1.0$, the roll moment is balanced by the active anti-roll moment, so φ is not influenced by the lateral acceleration variations, and $\delta \varphi = 0$ in the whole frequency range. For $k = 1.2$, the active anti-roll moment is larger than the roll moment, and the vehicle body rolls towards the inner side of the corner, which is confirmed by the steady-state value of the phase angle of 0 deg for $\delta \varphi$.

For two lateral accelerations, Figure 8 includes the Bode plots of $\delta r / \delta f$, for: (i) the complete Model 1 formulation (Total); (ii) Model 1, by imposing $C'_{i,0} = 0$; (iii) Model 1 with $F'_{y,i,0} = 0$; (iv) Model 1 with $C'_{i,0} = F'_{y,i,0} = 0$, i.e. the conventional bicycle model. The novel important insight is that the effect of $F'_{y,i,0}$ is much more significant than that of $C'_{i,0}$, which means that during the model development for anti-roll moment distribution control design, the focus should be on the lateral force variation induced by the active suspension system, rather than on the cornering stiffness variation.

5.2. Comparison of Models 1–4

Figure 9 compares the Bode plots of $\delta r / \delta f$ for Models 1–4 at $a_y = 3$ and 9 m/s², and $V = 100$ km/h. At $a_y = 3$ m/s² (Figure 9(a)), all models have similar trends both in magnitude

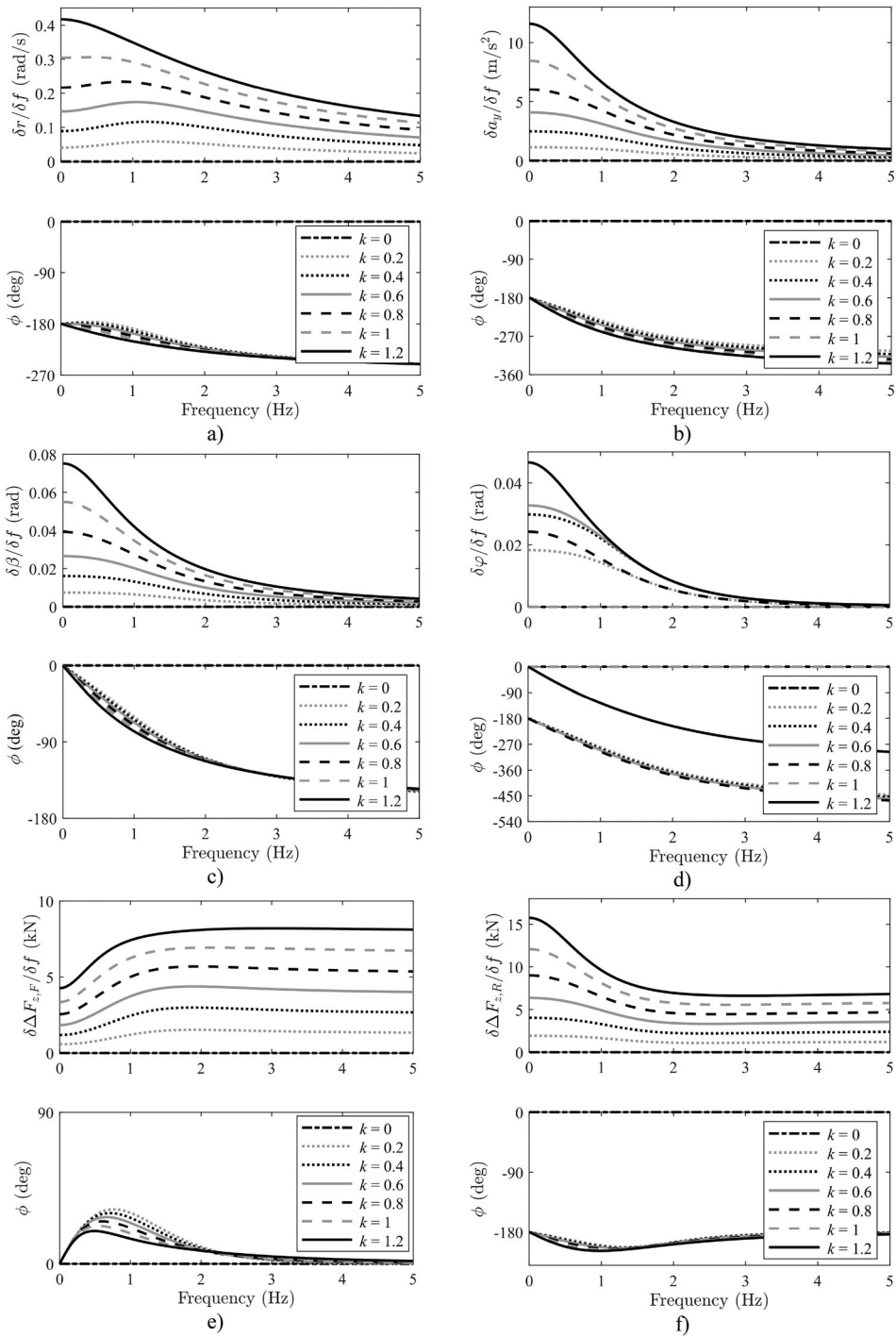


Figure 7. Bode plots of: (a) $\delta r / \delta f$; (b) $\delta a_y / \delta f$; (c) $\delta \beta / \delta f$; (d) $\delta \varphi / \delta f$; (e) $\delta \Delta F_{z,F} / \delta f$; and (f) $\delta \Delta F_{z,R} / \delta f$ for Model 1 linearised at $a_y = 6 \text{ m/s}^2$ and $V = 100 \text{ km/h}$

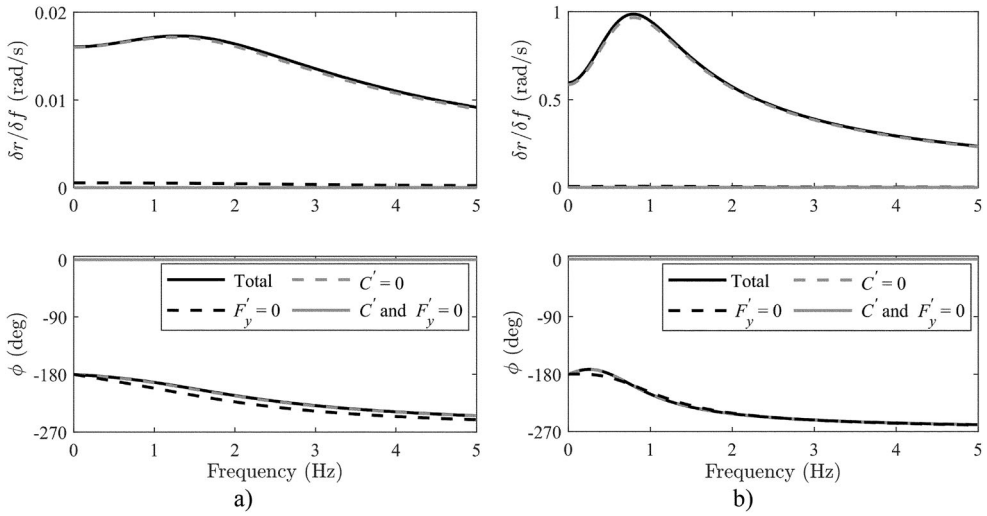


Figure 8. Bode plots of $\delta r/\delta f$ at $V = 100$ km/h for Model 1 at: (a) $a_y = 3$ m/s²; and (b) $a_y = 9$ m/s².

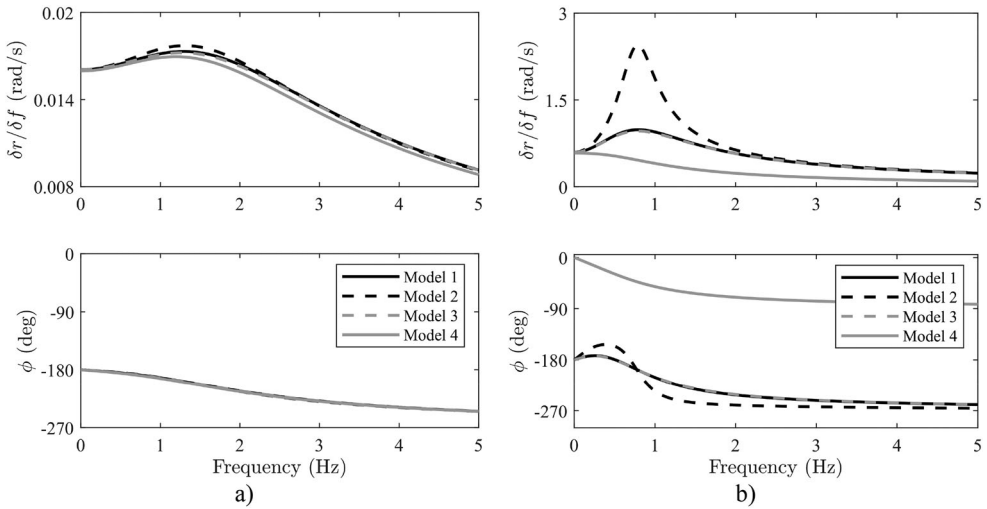


Figure 9. Bode plots of $\delta r/\delta f$ at $V = 100$ km/h for Models 1–4 at: (a) $a_y = 3$ m/s²; and (b) $a_y = 9$ m/s².

and phase. On the contrary, Figure 9(b), for $a_y = 9$ m/s², shows that Model 2 is characterised by an important resonance peak at frequencies lower than 1 Hz, and differs from Models 1 and 3 in the phase as well, although ϕ starts from the same value of -180 deg. The resonant behaviour of Model 2 is caused by the fact that its anti-roll moment is calculated from the yaw rate through (25), which provokes a coupling with the yaw rate response.

At $a_y = 9$ m/s², the axle cornering stiffness increases with the lateral load transfer, see Figure 3 for slip angles larger than 3 deg. Differently from the other models, Model 4 incorporates only the effect of the lateral load transfer on the axle cornering stiffness, and neglects the lateral axle force variation at the linearisation point, which is the prevalent

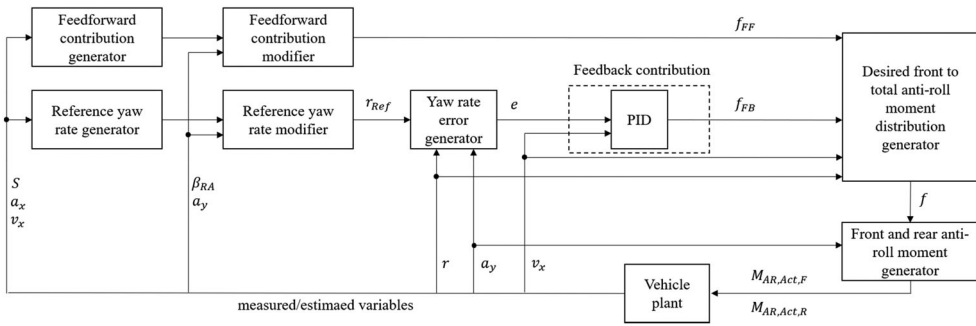


Figure 10. Simplified schematic of the anti-roll moment distribution controller.

effect, as discussed in Section 5.1. Therefore, Model 4 shows a steady-state phase shift of 180 deg with respect to the other models, i.e. to obtain the same yaw rate effect, it would suggest an opposite sign of the front-to-total anti-roll moment distribution control action. This important observation suggests that Model 4 is not suitable for control design at high lateral accelerations.

6. Feedback control design

6.1. Control structure

Figure 10 is a simplified schematic of the implemented front-to-total anti-roll moment distribution controller. f is given by the combination of two contributions: (i) a nonlinear feedforward contribution, f_{FF} , computed offline via an optimisation routine based on a quasi-static model, see [30] and [32–34], which provides the desired cornering response in nominal steady-state conditions; and (ii) a feedback contribution, f_{FB} , generated by a PI controller, which is the focus of this study.

The yaw rate error used as input to the feedback controller is given by $e = e_r \text{sgn}(a_y) = [r_{Ref} - r] \text{sgn}(a_y)$, where the sign function takes into account that the anti-roll moment distribution only has an indirect effect on the yaw moment, and such influence depends on the direction of the lateral load transfer. The feedback controller operates as a reverse acting controller, i.e. its gains are expected to be negative, as the increase of the vehicle yaw rate requires a decrease of the control action. The reference yaw rate, r_{Ref} , and the feedforward contribution, f_{FF} , are modified based on the value of the rear axle sideslip angle, β_{RA} , and a_y , to avoid unstable vehicle behaviour in critical conditions, see [30] and [36]. Starting from the resulting f , the front and rear anti-roll moment generator calculates the front and rear active anti-roll moments, $M_{AR,Act,F}$ and $M_{AR,Act,R}$, which are sent to the suspension actuators.

6.2. Feedback controller design

In the control design routine, the plant is modelled through the following transfer function:

$$G_{Plant} = G_{Veh}(s)G_{Act}(s) = \frac{\delta r}{\delta f}(s) \frac{e^{-\tau_1 s}}{\tau_2 s + 1} \quad (32)$$

where $G_{Veh}(s) = \delta r / \delta f$ is the vehicle response transfer function, obtained from the state-space formulations of Models 1–4; s is the Laplace operator; and $G_{Act}(s)$ is the suspension actuation transfer function, including a pure time delay τ_1 and first order dynamics with time constant τ_2 , tuned from experimental data of the specific actuators [30].

The open-loop and closed-loop transfer functions of the system, respectively $L(s)$ and $T(s)$, are given by

$$L(s) = G_{PI}G_{Plant} = \left[K_P + \frac{K_I}{s} \right] \frac{\delta r}{\delta f}(s) \frac{e^{-\tau_1 s}}{\tau_2 s + 1}$$

$$T(s) = \frac{L(s)}{1 + L(s)} \quad (33)$$

where K_P and K_I are the proportional and integral gains of the PI controller transfer function G_{PI} (the actual formulation also includes an anti-windup scheme).

The PI gains are obtained through a model-based optimisation routine, minimising a cost function J :

$$[K_P, K_I] = \arg \min(J)$$

$$J = W_1 \overline{t_r} + W_2 \overline{OS} + W_3 \overline{t_{set}} = W_1 \frac{t_r}{t_{r,chr}} + W_2 \frac{OS}{OS_{chr}} + W_3 \frac{t_{set}}{t_{set,chr}}$$

$$\text{s.t. } GM > GM_{min}, PM > PM_{min} \quad (34)$$

where $\overline{t_r}$, \overline{OS} and $\overline{t_{set}}$ are the rise time, overshoot and settling time for a step input test, calculated from $T(s)$, and scaled with appropriate characteristic values, respectively $t_{r,chr}$, OS_{chr} and $t_{set,chr}$; W_1 , W_2 and W_3 are weights; and GM and PM are the gain and phase margins, obtained from $L(s)$ and constrained to be larger than recommended values for system stability (see [37]), i.e. $GM_{min} = 2$ and $PM_{min} = 30$ deg. The Matlab *fmincon* function is used to solve the optimisation problem in (34).

6.3. Model-based control gains

The routine of Section 6.2 was used in conjunction with Models 1–4, to obtain four sets of PI controller gains, each one for three values of lateral acceleration (i.e. 3, 6 and 9 m/s²) and speed (i.e. 60, 80 and 100 km/h), see Table 3.

Once designed with the respective model, the gains based on Models 1–4 were verified with Model 1 in terms of GM and PM values (see the last six columns on the right of the table). Model 1 was adopted as reference plant since it: (i) incorporates the more reliable lateral axle force model (Model A), according to the analysis in Section 3; and (ii) uses the industrially adopted expression of the anti-roll moment as a function of lateral acceleration. The subscripts 3, 6 and 9 in the gain and phase margin notations indicate the lateral acceleration level (in m/s²) at which Model 1 is linearised for margin computation.

The following observations can be made:

- Models 1–3 generate very similar sets of gains, i.e. the total anti-roll moment formulation does not have a major impact.

- The gains calculated for low lateral accelerations are higher (in absolute value) than those generated for high lateral accelerations. In particular, the gains for $a_y = 3 \text{ m/s}^2$ tend to make the system based on the same model formulation unstable at 6 and 9 m/s^2 . In the table, this is only shown for Model 1, but it was also verified for Models 2–4. The important conclusion is that gains designed for low lateral acceleration cannot be used at larger a_y .

Table 3. Controller gains based on Models 1–4, according to the routine in Section 6.2; gain and phase margins assessed a-posteriori with Model 1 linearised at $a_y = 3, 6$ and 9 m/s^2 .

		Gains computed with Model 1				$a_y = 3 \text{ m/s}^2$		$a_y = 6 \text{ m/s}^2$		$a_y = 9 \text{ m/s}^2$	
a_y used for gain computation [m/s^2]	V [km/h]	K_P [s/rad]	K_I [1/rad]	GM_3 [-]	PM_3 [deg]	GM_6 [-]	PM_6 [deg]	GM_9 [-]	PM_9 [deg]		
Model 1 based gains evaluated with Model 1											
3	60	-475.8	-4871.9	2.35	50.21	0.21	-90.4	1.86	-100.42		
	80	-244.9	-2193.9	2.09	39.40	0.20	-88.5	2.85	-153.85		
	100	-112.9	-790.7	2.62	49.55	0.26	-70.84	5.22	-145.95		
6	60	-49.9	-590.9	21.65	91.31	2.00	36.52	0.27	-61.57		
	80	-27.3	-151.6	20.21	97.89	2.01	36.81	0.44	-39.11		
	100	-16.1	-58.8	19.81	101.29	2.00	35.26	0.65	-20.65		
9	60	-7.6	-28.2	165.15	91.13	15.43	102.77	2.25	40.22		
	80	-4.9	-12.5	117.19	91.98	11.66	112.51	2.64	46.22		
	100	-3.4	-9.7	93.71	92.59	9.47	122.31	3.07	50.31		
Gains computed with Model 2											
a_y used for gain computation [m/s^2]	V [km/h]	K_P [s/rad]	K_I [1/rad]	GM_3 [-]	PM_3 [deg]	GM_6 [-]	PM_6 [deg]	GM_9 [-]	PM_9 [deg]		
Model 2 based gains evaluated with Model 1											
3	60	-567.1	-1764.0	2.24	53.67	0.21	-100.12	1.57	-76.34		
	80	-206.3	-921.7	2.73	60.23	0.27	-74.85	3.40	-173.76		
	100	-80.4	-1381.3	2.75	38.44	0.26	-58.01	7.27	-122.42		
6	60	-44.4	-192.4	28.12	96.17	2.62	60.79	0.38	-49.98		
	80	-18.7	-75.9	30.43	96.42	3.02	62.29	0.68	-18.57		
	100	-9.0	-34.3	35.32	96.21	3.56	65.63	1.15	6.55		
9	60	-4.5	-17.1	279.19	90.66	26.09	97.45	3.82	66.41		
	80	-3.2	-6.3	186.42	91.32	18.56	104.69	4.22	69.39		
	100	-2.5	-3.6	133.22	92.08	13.51	115.17	4.41	68.81		
Gains computed with Model 3											
a_y used for gain computation [m/s^2]	V [km/h]	K_P [s/rad]	K_I [1/rad]	GM_3 [-]	PM_3 [deg]	GM_6 [-]	PM_6 [deg]	GM_9 [-]	PM_9 [deg]		
Model 3 based gains evaluated with Model 1											
3	60	-571.2	-2858.9	2.16	49.46	0.20	-101.45	1.56	-74.91		
	80	-203.3	-1419.3	2.64	54.78	0.26	-75.22	3.44	-174.64		
	100	-106.1	-781.8	2.77	51.94	0.27	-67.25	5.56	-140.68		
6	60	-54.8	-75.2	23.86	100.07	2.23	51.62	0.33	-60.53		
	80	-22.1	-50.9	26.56	99.00	2.64	55.99	0.60	-25.51		
	100	-11.2	-26.7	29.25	98.69	2.96	57.57	0.96	-1.78		
9	60	-5.8	-14.4	221.34	90.97	20.71	100.87	3.05	57.04		
	80	-3.9	-9.5	150.07	91.56	14.93	107.52	3.38	57.91		
	100	-2.8	-7.3	114.88	92.17	11.62	116.71	3.77	59.44		

(continued).

Table 3. Continued.

a_y used for gain computation [m/s ²]	V [km/h]	Gains computed with Model 4		$a_y = 3 \text{ m/s}^2$		$a_y = 6 \text{ m/s}^2$		$a_y = 9 \text{ m/s}^2$	
		K_P [s/rad]	K_I [1/rad]	GM_3 [-]	PM_3 [deg]	GM_6 [-]	PM_6 [deg]	GM_9 [-]	PM_9 [deg]
Model 4 based gains evaluated with Model 1									
3	60	-850.1	-4630.4	1.44	22.32	5.68	-134.03	1.04	-171.38
	80	-295.6	-334.9	2.03	42.88	0.20	-98.31	2.38	-133.25
	100	-97.1	-604.5	3.11	60.06	0.31	-61.28	6.07	-132.89
6	60	-55.6	-654.7	19.42	91.51	1.79	30.80	0.25	-67.78
	80	-23.9	-105.1	23.62	97.92	2.34	46.66	0.53	-31.28
	100	-10.5	-19.9	31.34	98.51	3.17	62.28	1.03	1.62
9	60	60.2	163.6	231.93	-80.15	22.9	-137.21	4.13	-112.99
	80	20.0	20.0	354.26	-80.93	37.29	-114.32	9.80	-160.81
	100	17.4	19.9	244.12	-75.09	26.17	-144.22	9.47	-157.86

- The gains calculated with Models 1–3 for $a_y = 9 \text{ m/s}^2$ provide stable performance at lower lateral accelerations, at which they are conservative, i.e. they are associated with higher values of gain and phase margins than the optimal gains for that a_y value. As lateral acceleration can swiftly vary with time, which can provoke stability issues in a gain scheduling scheme, for the time domain analysis no gain scheduling was implemented with a_y , and the gains calculated at 9 m/s^2 with Models 1–3 were used along the whole lateral acceleration range.
- The gains based on Model 4 for $a_y = 9 \text{ m/s}^2$ have opposite sign from those obtained with Models 1–3, and make the system unstable for all lateral accelerations according to all the other (more realistic) models, which highlights the major limitation of Model 4.
- The gains calculated for low vehicle speed are larger (in absolute value) than those for high vehicle speed, even if their variation with V is much less important than that with a_y . The gain variation with V is associated with the yaw damping level of the vehicle transfer function, which decreases with speed. As during driving the variation of V is normally slower than the variation of a_y , it was decided to implement a gain scheduling scheme as a function of V .

7. Simulation results

7.1. Experimentally validated model and simulation set-up

The dynamic behaviour of the case study electric vehicle was simulated with an experimentally validated nonlinear vehicle dynamics model, implemented in Matlab-Simulink. The model includes a magic formula (version 5.2) tyre model with relaxation length, sprung mass dynamics (longitudinal, lateral, roll and yaw degrees of freedom) and wheel dynamics [30]. Figure 11 reports a selection of model validation results against experimental data, for the passive vehicle, i.e. without active suspension system, during: (i) a skipad test, see subplots (a) and (b), including the understeer characteristic and rear axle sideslip angle characteristic; and (ii) a sinusoidal steering test, see subplots (c), (d) and (e), with the time histories of lateral acceleration, yaw rate and sideslip angle. Given the good match between

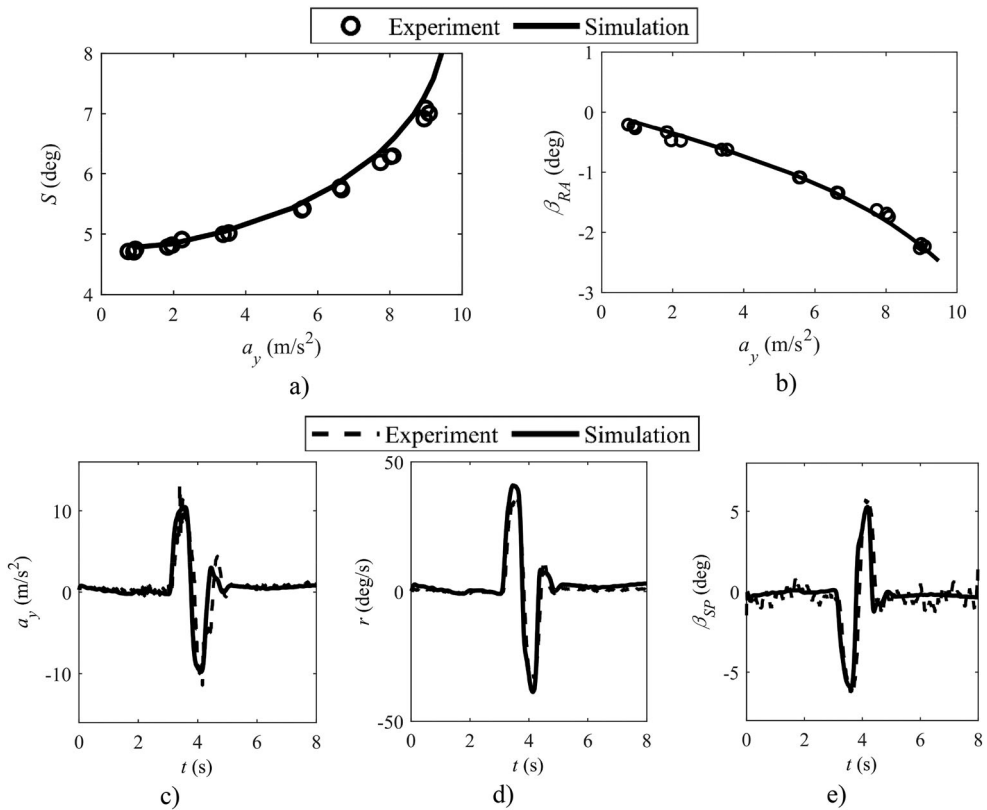


Figure 11. Model validation results during a skidpad test (a) and (b) and a sinusoidal steering test (c), (d) and (e), in terms of: (a) understeer characteristic; (b) rear axle sideslip angle characteristic; (c) lateral acceleration profile; (d) yaw rate profile; (e) sideslip angle profile at the sensor attachment point (rear bumper).

simulations and experiments in quasi-steady-state and transient conditions, the model can be considered a reliable tool for control system assessment.

To evaluate how the choice of the model-based feedback controller gains influences the vehicle behaviour, the controllers from Section 6 are compared along vehicle simulations. Similarly to the approach in Table 3, in the time domain comparison of the different model-based PI controllers, it was decided to use the Model 1 formulation of the total anti-roll moment, starting from a_y (see Figure 10), since it is the one commonly implemented in production systems. In any case, it was verified that the total anti-roll moment formulation does not have any major impact on the results. As the gains obtained by linearising Models 1–3 at $a_y = 9 \text{ m/s}^2$ lead to a stable system in any cornering condition according to the frequency domain analysis, in the following results the controllers based on Models 1–3 adopt the gains for $a_y = 9 \text{ m/s}^2$ (see Table 3). Instead, for the PI controller based on Model 4, the simulations are carried out for three cases: (i) PI gains obtained for $a_y = 9 \text{ m/s}^2$, indicated as Model 4a in the remainder; (ii) PI gains for $a_y = 6 \text{ m/s}^2$ (Model 4b); and (iii) PI gains for $a_y = 3 \text{ m/s}^2$ (Model 4c).

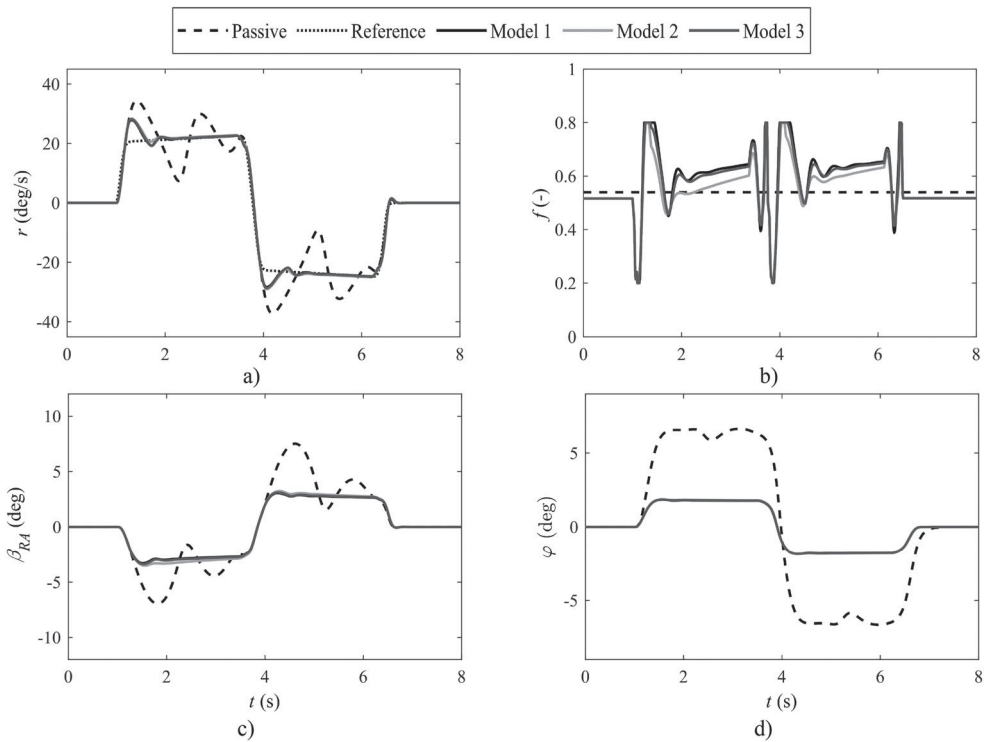


Figure 12. Multiple step steer results for the passive vehicle and the vehicle with the controllers based on Models 1-3, from an initial speed of 100 km/h, in terms of time profiles of: (a) r ; (b) f ; (c) β_{RA} ; and (d) φ .

In the following analyses, to highlight the effect of the front-to-total anti-roll moment distribution controller, the stability controller based on the actuation of the friction brakes and the torque-vectoring controller using the individually controlled electric motors are both deactivated.

7.2. Multiple step steer

Figures 12 and 13 report the time histories of the main variables during a multiple step steer test from an initial speed of 100 km/h, with high tyre-road friction conditions, for the passive vehicle and the same vehicle with the front-to-total anti-roll moment distribution controllers based on Models 1–3 and Models 4a–4c. The simulated manoeuvre consists of a first swift steering wheel angle variation from 0 deg to 150 deg, a second one from 150 deg to -150 deg, and a final one that brings the steering wheel angle back to 0 deg. All steering angle variations are performed with a gradient of 400 deg/s. During the manoeuvre, the total tractive torque demand is set to zero.

The results for the controllers based on Models 1–3 highlight a significant improvement of the vehicle response, namely reduced overshoots and settling times of the yaw rate and sideslip angle, in comparison with the passive vehicle, see Figure 12(a,c). Figure 12(b,d) shows the front-to-total anti-roll moment distribution control actions and the vehicle roll angle, where the magnitude of the latter is also consistently lower than for the passive

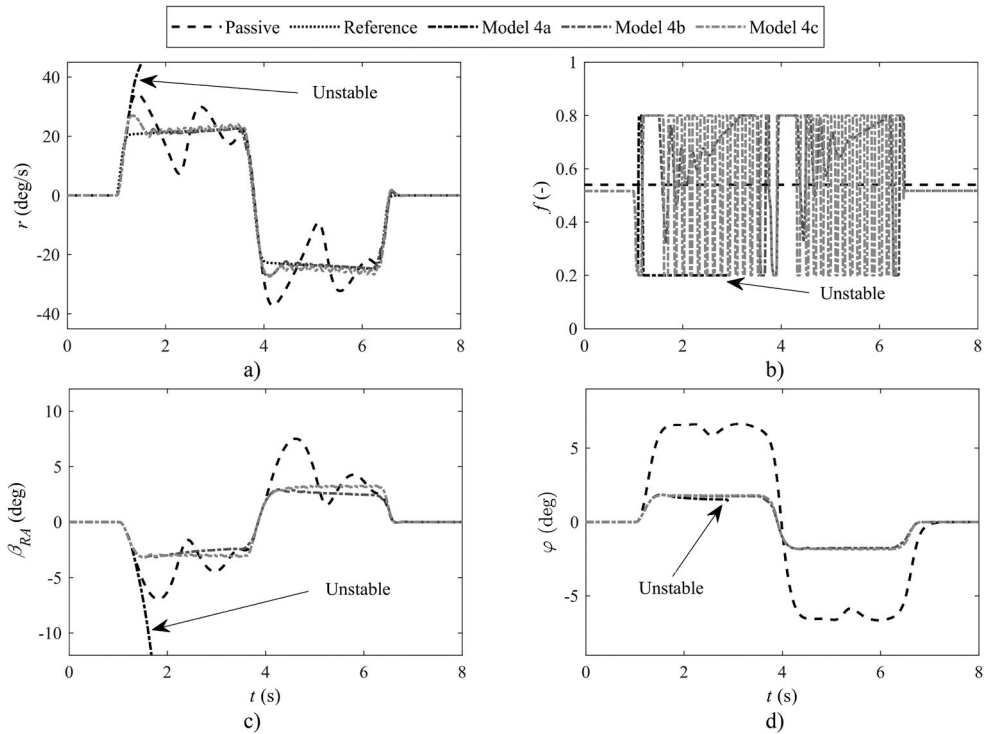


Figure 13. Multiple step steer results for the passive vehicle and the vehicle with the controllers based on Models 4a-c, from an initial speed of 100 km/h, in terms of time profiles of: (a) r ; (b) f ; (c) β_{RA} ; and (d) φ .

Table 4. RMS and peak values of the yaw rate error and rear axle sideslip angle for the passive vehicle and the vehicle with controllers based on the different models.

	Model 1	Model 2	Model 3	Model 4a*	Model 4b	Model 4c	Passive
$RMS(e_r)$ (deg/s)	1.19	1.28	1.24	13.03	1.11	1.10	4.35
$\max(e_r)$ (deg/s)	7.19	7.69	7.48	51.74	6.29	6.23	15.59
$RMS(\beta_{RA})$ (deg)	1.58	1.69	1.60	8.21	1.51	1.72	2.53
$\max(\beta_{RA})$ (deg)	3.28	3.52	3.36	46.86	3.17	3.28	7.51

*Notes: The specific vehicle configuration has unstable behaviour (the simulation is interrupted when $|\beta|$ reaches 40 deg).

configuration. The general improvement of vehicle response is confirmed by the objective performance indicators in Table 4, reporting the root mean square values of the yaw rate error and rear axle sideslip angle, $RMS(e_r)$ and $RMS(\beta_{RA})$, as well as the respective maximum absolute values, $\max(|e_r|)$ and $\max(|\beta_{RA}|)$, for the passive vehicle and each of the six controlled cases. For example, the controller based on Model 1 brings an $RMS(e_r)$ of 1.19 deg/s, against the 4.35 deg/s of the passive configuration, and a maximum $|\beta_{RA}|$ value of 3.28 deg, against the 7.51 deg of the passive counterpart. This kind of benefits is comparable to those achievable with a stability controller in similar conditions.

On the contrary, the controllers based on Model 4 show the stability issues highlighted during the design phase in the frequency domain. In fact, the vehicle with the controller based on Model 4a has divergent yaw rate and sideslip behaviour, visible in Figure 13 as

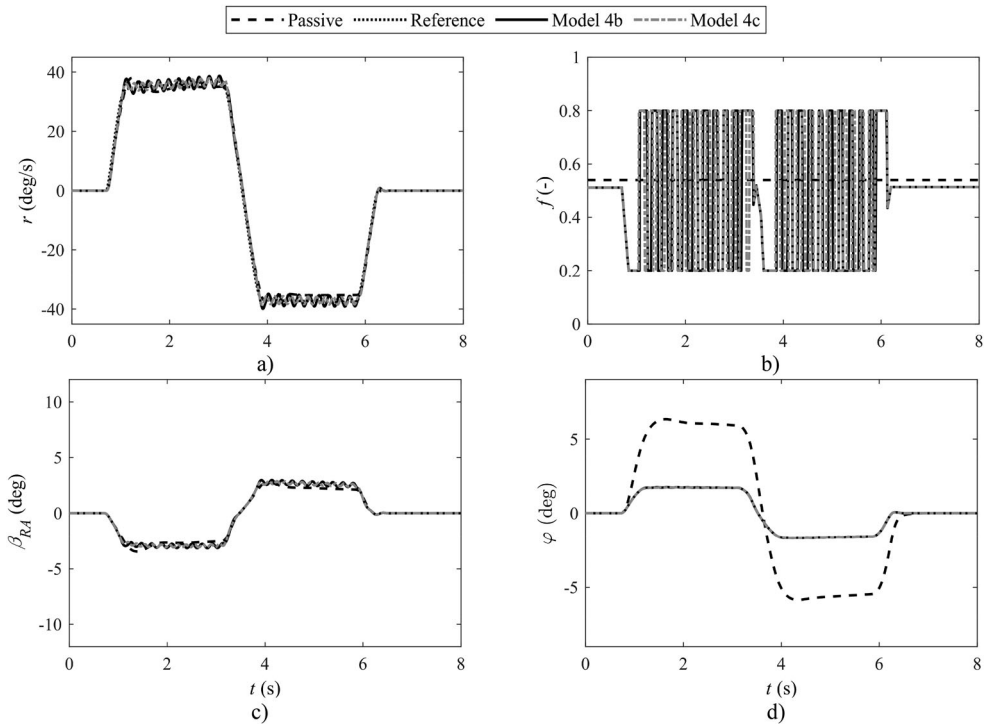


Figure 14. Multiple step steer results for the passive vehicle and the vehicle with the controller based on Models 4b and 4c, from an initial speed of 60 km/h, in terms of time profiles of: (a) r ; (b) f ; (c) β_{RA} ; and (d) φ .

well as from the RMS and peak values in Table 4. Although the vehicle with the Model 4c based controller provides a safe cornering response, significantly enhanced with respect to that of the passive configuration, it is characterised by high amplitude and high frequency oscillations of the control action, see the f profile (indicated by the grey dash dotted line) in Figure 13(b), which provoke marginal yaw rate and sideslip angle ripples, compromising the comfort benefit of active roll control. At 100 km/h, the controller based on Model 4b provides desirable behaviour without control action oscillations, but when tested at 60 km/h (see Figure 14), speed at which the gain and phase margin analysis using Model 1 indicates stability problems (see Table 3), it presents similar control action oscillations to those of the controller based on Model 4c for 100 km/h; moreover, both controllers show increased yaw rate oscillations at 60 km/h. This confirms the importance of using reliable models, i.e. Models 1-3, for anti-roll moment distribution control design, and the general unsuitability of Model 4.

7.3. Sine-with-dwell test

The sine-with-dwell is the standard test for assessing the performance of vehicle stability controllers [38], and consists of a series of manoeuvres with a pre-defined steering input, i.e. the so-called sine-with-dwell, carried out at increasing steering wheel angle amplitudes,

Table 5. RMS and peak values of the yaw rate error and rear axle sideslip angle during the last run of the sine-with-dwell test for the passive vehicle and the vehicle with controllers based on the different models.

	Model 1	Model 2	Model 3	Model 4a*	Model 4b	Model 4c	Passive*
$RMS(e_r)$ (deg/s)	2.13	2.28	2.22	23.36	1.99	2.07	16.82
$\max(e_r)$ (deg/s)	12.90	13.69	13.31	92.68	11.45	12.74	56.02
$RMS(\beta_{RA})$ (deg)	1.21	1.23	1.24	6.85	1.09	1.17	11.24
$\max(\beta_{RA})$ (deg)	3.75	3.87	3.81	44.95	3.54	3.72	43.10

*Notes: The specific vehicle configuration has unstable behaviour (the simulation is interrupted when $|\beta|$ reaches 40 deg).

obtained by scaling up the steering wheel angle required to generate a lateral acceleration of 0.3 g at 80 km/h.

A test run is successful if the vehicle exceeds a specified lateral displacement, and the yaw rate is below appropriate thresholds at specific times. The passive vehicle configuration passes the test up to ~ 110 deg of steering wheel input.

Remarkably, all implemented suspension controller configurations, with the exception of the one based on Model 4a, successfully completed the test series, with the last test being the one with a steering wheel angle amplitude of 280 deg. Table 5 reports the performance indicators for all vehicle configurations for the last run of the sine-with-dwell test series. The passive vehicle becomes unstable during the second part of the test, after the steering wheel input is reversed. The controllers based on Models 1–3 provide consistently stable behaviour, while the controllers based on Models 4a and 4c have similar response to the one observed in the multiple step steer test, with respectively unstable vehicle behaviour and good vehicle response but with significant control action oscillations.

8. Conclusions

This study analysed the effect of the lateral load transfer on the lateral axle force in passenger cars, and compared linearised axle and vehicle dynamics model formulations for front-to-total anti-roll moment distribution control design in the frequency domain. The main conclusions are:

- (1) The lateral load transfer always causes a reduction of the lateral axle force. However, depending on the slip angle value, the axle cornering stiffness, defined as the incremental ratio of the lateral force with respect to slip angle for a given load transfer, can decrease or increase. In particular, rather interestingly, the axle cornering stiffness tends to increase with the load transfer at medium-to-high slip angles, i.e. in the typical conditions in which an active suspension system can be beneficial to the vehicle cornering response.
- (2) The conventional simplified model from the literature for front-to-total anti-roll moment distribution control design is based on a linear relationship between lateral force and slip angle, with a quadratic variation of the axle cornering stiffness with the lateral load transfer; hence, its formulation is nonlinear, and for frequency domain analysis requires linearisation, which, to the best of our knowledge, has not been presented yet. Such model is effective in capturing the cornering stiffness variation with the load transfer; however, it does not directly consider the variation of the lateral axle force for a given slip angle, which, based on our results, is the prevalent effect to be

considered in anti-roll moment distribution control design. To cover this gap, a linearised lateral axle force model formulation was derived and compared with the magic formula, showing consistently good performance for slip angle and vertical tyre load variations around multiple linearisation points.

- (3) Novel linearised single-track vehicle model formulations, based on the proposed linearised lateral axle force model, were presented, and compared in the frequency domain with a linearised single-track vehicle model including the quadratic axle cornering stiffness model from the literature. Results show the importance of the correct and concurrent modelling of the effects of the slip angle and lateral load transfer variations, especially at the limit of handling.
- (4) The gain and phase margin analysis shows that controllers designed through the linearised model considering only the cornering stiffness variation with the lateral load transfer, and not the lateral axle force variation, can be unstable at high lateral accelerations. This is confirmed by the set of simulation results of multiple step steer and sine-with-dwell tests, in which the vehicle configurations with the front-to-total anti-roll moment distribution controllers based on the proposed linearised lateral axle force formulation complete the full set of tests, without requiring the intervention of the stability controller using the friction brakes. On the contrary, the controller designs based on lateral axle force models considering only the variation of the axle cornering stiffness are characterised by stability issues, either in the form of divergent vehicle cornering behaviour, or in the form of significant undamped control action oscillations.

Disclosure statement

No potential conflict of interest was reported by the authors.

Funding

This work was supported by H2020 Marie Skłodowska-Curie Actions under grant 734832 (CLOVER project).

References

- [1] Pacejka HB. *Tire and vehicle dynamics*. Oxford: Elsevier; 2005.
- [2] Danesin D, Krief P, Sorniotti A, et al. Active roll control to increase handling and comfort. SAE Technical Paper 2003-01-0962, 2003.
- [3] Clover C, Bernard J. The influence of lateral load transfer distribution on directional response. SAE Technical Paper 930763, 1993.
- [4] Čorić M, Deur J, Kasak J, et al. Optimisation of active suspension control inputs for improved vehicle handling performance. *Veh Syst Dyn*. 2016;54(11):1574–1600.
- [5] Čorić M, Deur J, Xu L, et al. Optimisation of active suspension control inputs for improved performance of active safety systems. *Veh Syst Dyn*. 2018;56(1):1–26.
- [6] Williams DE, Haddad WM. Nonlinear control of roll moment distribution to influence vehicle yaw characteristics. *IEEE Trans on Control Syst Technol*. 1995;3(1):110–116.
- [7] Wang J, Wilson DA, Xu W, et al. Active suspension control to improve vehicle ride and steady-state handling. *IEEE Conference on Decision and Control*, 2005.
- [8] Shim T, Margolis D. Dynamic normal force control for vehicle stability enhancement. *Int J Veh Auton Syst*. 2005;3(1):1–14.

- [9] Elbeheiry EM, Zeyada YF, Elaraby ME. Handling Capabilities of Vehicles in Emergencies using Coordinated AFS and ARMC systems. *Veh Syst Dyn.* 2001;35(3):195–215.
- [10] Varnhagen S, Anubi OM, Sabato Z, et al. Active suspension for the control of planar vehicle dynamics. *IEEE International Conference on Systems, Man, and Cybernetics (SMC)*, 2014.
- [11] Yamamoto M. Active Control Strategy for Improved Handling and Stability. SAE Technical Paper 911902, 1991.
- [12] Furukawa Y, Abe M. Advanced chassis control systems for vehicle handling and active safety. *Veh Syst Dyn.* 1997;28(2-3):59–86.
- [13] Badji B, Fenaux E, El Bagdouri M, et al. Nonlinear single track model analysis using Volterra series approach. *Veh Syst Dyn.* 2009;47(1):81–98.
- [14] Cho W, Choi J, Kim C, et al. Unified chassis control for the improvement of agility, maneuverability, and lateral stability. *IEEE Trans Veh Technol.* 2012;61(3):1008–1020.
- [15] Shin M, Bae S, Lee JM, et al. New vehicle dynamics model for yaw rate estimation. *Veh Syst Dyn Sup.* 2002;37:96–106.
- [16] Li L, Jia G, Chen J, et al. A novel vehicle dynamics stability control algorithm based on the hierarchical strategy with constrain of nonlinear tyre forces. *Veh Syst Dyn.* 2015;53(8):1093–1116.
- [17] Genta G. *Motor vehicle dynamics: modeling and simulation*. 1st ed. Singapore: World Scientific; 1997.
- [18] Jialing Y, Shan R, Zhihong L, et al. Improving lateral stability by distributing roll moment via semi-active suspension. *FISITA World Automotive Congress*, 2016.
- [19] Chu TW, Jones RP. Analysis and simulation of nonlinear handling characteristics of automotive vehicles with focus on lateral load transfer. *Veh Syst Dyn.* 2008;46(1):17–31.
- [20] Bodie MO, Hac A. Closed loop yaw control of vehicles using magneto-rheological dampers. SAE Technical Paper 2000-01-0107, 2000.
- [21] Lakehal-Ayat M, Diop S, Fenaux E. An improved active suspension yaw rate control. *American Control Conference*, 2002.
- [22] Wu L, Ma F, Pu Y, et al. Integrated Effects of Active Suspension and Rear-Wheel Steering Control Systems on Vehicle Lateral Stability. SAE Technical Paper 2017-01-0257, 2017.
- [23] Xu Y, Ahmadian M. Improving the capacity of tire normal force via variable stiffness and damping suspension system. *J of Terramechanics.* 2013;50(2):122–132.
- [24] Gerhard J, Laiou MC, Monnigmann M, et al. Robust yaw control design with active differential and active roll control systems. *IFAC Proc.* 2005;38(1):73–78.
- [25] Xinpeng T, Xiaocheng D. Simulation and study of active roll control for SUV based on fuzzy PID. SAE Technical Paper 2007-01-3570, 2007.
- [26] Abe M. A study on effects of roll moment distribution control in active suspension on improvement of limit performance of vehicle handling. *Int J of Veh Design.* 1994;15(3/4/5):326–336.
- [27] Cooper N, Crolla D, Levesley M. Integration of active suspension and active driveline to ensure stability while improving vehicle dynamics. SAE Technical Paper 2005-01-0414, 2005.
- [28] Yan M, Pi D, Li Y, et al. The design of anti-roll moment distribution for dual-channel active stabilizer bar system. *Chinese Control and Decision Conference*, 2018.
- [29] Termousa H, Shraima H, Taljb R, et al. Coordinated control strategies for active steering, differential braking and active suspension for vehicle stability, handling and safety improvement. *Veh Syst Dyn.* 2019;57(10):1494–1529.
- [30] Ricco M, Zanchetta M, Cardolini Rizzo G, et al. On the design of yaw rate control via variable front-to-total anti-roll moment distribution. *IEEE Trans on Vehicular Technol.* 2020;69(2):1388–1403.
- [31] Guiggiani M. *The science of vehicle dynamics*. 2nd ed. Dordrecht: Springer; 2018.
- [32] Chatzikomis C, Sornioti A, Gruber P, et al. Torque-vectoring control for an autonomous and driverless electric racing vehicle with multiple motors. *SAE Int J Veh Dyn Stab and NVH.* 2017;1(2):338–351.
- [33] De Novellis L, Sornioti A, Gruber P. Optimal wheel torque distribution for a four-wheel-drive fully electric vehicle. *SAE Int J Passen Cars Mech Syst.* 2013;6(1):128–136.

- [34] De Novellis L, Sorniotti A, Gruber P. Design and comparison of the handling performance of different electric vehicle layouts. *Proc Inst Mech Eng Part D: J Automob Eng.* 2013;228(2):218–232.
- [35] Milliken WF, Milliken DL. *Race Car vehicle dynamics*. Warrendale (PA): SAE International; 1994.
- [36] Lenzo B, Sorniotti A, Gruber P, et al. On the experimental analysis of single input single output control of yaw rate and sideslip angle. *Int J of Automot Technol.* 2017;18(5):799–811.
- [37] Skogestad S, Postlethwaite I. *Multivariable feedback control: analysis and design*. 2nd ed. Chichester: Wiley; 2007.
- [38] FMVSS 126. *Federal Register.* 72(66):2007.